Yield decomposition and excitation energy reconstruction in an incomplete fusion reaction

A. Chbihi, L. G. Sobotka, Z. Majka,* D. G. Sarantites, D. W. Stracener, V. Abenante, T. M. Semkow,† and N. G. Nicolis
Department of Chemistry, Washington University, St. Louis, Missouri 63130

D. C. Hensley, J. R. Beene, and M. L. Halbert
Oak Ridge National Laboratory, Oak Ridge, Tennessee 37830
(Received 12 July 1990)

The velocity distribution of fusionlike products formed in the reaction 701 MeV $^{28}Si+^{100}Mo$ is decomposed into 26 incomplete fusion channels. If Coulomb corrections are neglected the yields of the incomplete fusion channels correlate much better with the Q value for projectile fragmentation than with the Q value for incomplete fusion. However, the correlation is much improved for incomplete fusion if a Coulomb correction is included. The partition of linear momentum between various sources is deduced using the measured residue velocity, multicomponent fits to light charged particle spectra, and mean neutron multiplicities. This reconstruction indicates that a substantial fraction of the momentum is not detected by our apparatus when slow residues are produced. With reasonable assumptions about this missing momentum component, the initial excitation of the compoundlike system is calculated as a function of the residue velocity.

I. INTRODUCTION

The decline of the complete fusion cross section in heavy-ion reactions as the relative velocity at contact exceeds $\frac{1}{10}c$ is well known. The telltale sign of this decline is found in measurements of the velocity distributions of the fusionlike residues[1] (ER) or in measurements of the angle between fission fragments.[2] In the former case the velocity distributions are broad and skewed to low velocities with mean values less than expected for complete momentum transfer. Coarsely, one can divide the explanations for this incomplete momentum transfer into those where the projectile nucleons carrying the nonfusing momentum traverse the target nucleus, and those where they do not. The latter, most appropriate for large impact parameters, was first provided by the sum-rule model of Wilczyński.[3] Here the projectile fragments into two pieces, one which fuses and the other which continues on a Coulomb trajectory with a velocity close to that of the beam. In this model, the nonfusing mass provides a crude impact parameter selection. On the other hand, for small impact parameters, one must account for incomplete fusion by lack of sufficient stopping power to thermalize the relative kinetic energy within the nuclear volume. Preequilibrium models of this sort have taken several forms, including Fermi jets,[4,5] hotspot formation[6,7] and the standard preequilibrium model[8] modified for heavy-ion systems.[9] More recently, Harvey has generated a model based on free nucleon-nucleon scattering.[10] This model may be valid over a broad range of impact parameters, but is undoubtedly restricted to high-energy heavy-ion collisions due to the lack of an explicit treatment of Pauli blocking. Another recent and promising development is the melding of the Fermi jet model to the nucleon exchange model developed for lower energy deep inelastic heavy-ion collisions.[11] The relevance of the different mechanisms underlying those models is one of the fundamental issues in the study of intermediate energy heavy-ion reactions. This is so, not simply because we wish to understand why complete fusion ceases to be viable, but also because of the restrictions imposed by these mechanisms on our capabilities of forming and therefore studying highly excited and rapidly rotating nuclear systems.

In this work we make two contributions to the understanding of the nature of the incomplete fusion process. The first contribution involves the properties of incomplete fusion (IF) channels, defined by the exclusive charge (Z_{ch}) and associated mass (A_{ch}) which compose the forward spray of particles, and the second contribution is to reconstruct the momentum, energy and mass partition as a function of residue velocity. The data presented here are from the reaction 701 MeV $^{28}Si+^{100}Mo$. Certain facets of this work have been presented previously[12] and the extracted excitation energies along with the evaporation spectra are used in the accompanying paper to investigate the level density of highly excited nuclei.[13]

II. EXPERIMENTAL

This study used a multilayered coincidence apparatus capable of detecting all of the emissions associated with fusionlike events. These include (a) the evaporation residue; (b) the nonfusing components which, as stated above, specify the channel; and (c) the products which result from the deexcitation of the highly excited, rapidly rotating, compound system (mostly n, p, α, and γ's). These diverse needs are served by a detection scheme incorporating (a) a forward annular parallel plate avalanche counter (PPAC) spanning 2.1° to 8.1° in the laboratory; (b) a forward wall of 35 plastic-CsI scintillators subtending angles between approximately 11° and 35°; and (c) a

small ball of 64 plastic-CsI scintillators subtending angles larger than approximately 35°, which is positioned inside a large multielement NaI ball. These experiments were done at the Holifield Heavy Ion Research Facility at Oak Ridge National Laboratory, where the 72 element NaI Spin Spectrometer was used to detect the penetrating γ's and neutrons.[14] In this work, the most forward NaI elements were removed in order to make room for an enlarged scattering chamber to house the CsI Wall and the PPAC. Therefore, only 65 of the 72 Spin Spectrometer elements were used, corresponding to 88% of 4π. The plastic-CsI multidetector system, which we call the Dwarf Ball and Wall, gives particle identification by utilizing the particle dependence of the time characteristics of the scintillation output. For the present study, each plastic-CsI module provides light charged particle identification (LCP=p, d, t, and α), distinguishes these LCP's from heavy ions (HI) and provides an energy for the LCP's. No heavy-ion identification was done due to the limited HI statistics obtained in these experiments. The energy calibration for LCP was obtained from elastic and inelastic scattering of 17 and 25 MeV protons on a ^{12}C target. The details of the Dwarf system are discussed in Ref. 15.

The event trigger was generated by any coincidence between the PPAC and the Dwarf system. The PPAC was positioned 285 mm downstream of the target (306 μg/cm^3, enriched to 97.3% ^{100}Mo). The time of the PPAC signal relative to the cyclotron radio frequency pulse and the PPAC pulse height were recorded for each event. A two-dimensional map of these parameters is shown in Fig. 1. The tall steep mountain at large times and small pulse height results from elastic scattering events. The locus for fusionlike events is the long arc extending from small times and small pulse heights to large times and large pulse heights. Only the data in this arc are analyzed in this work. The time resolution estimated from the full width at half maximum of the elastic peak is approximately 3 ns. This resolution is more than adequate for this work since no mass information was extracted from the timing information, only coarse binning of the velocity spectrum is done.

III. INCOMPLETE FUSION CHANNELS

We have identified 26 channels differing by their forward ($\theta_{lab} < 35°$) light charged particle (LCP) composition. These channels consist of 1, 2, 3, and 4 LCP's. The ER velocity distributions are shown in Fig. 2 for selected channels and for the sum of all charged particle channels (top). The latter distribution should be quite similar to the inclusive distribution (omitting only xn channels). The most probable velocity, 77% of the full momentum transfer value, is consistent with the systematics presented in Ref. 1. These distributions can be understood as consisting of two components. One of these components,

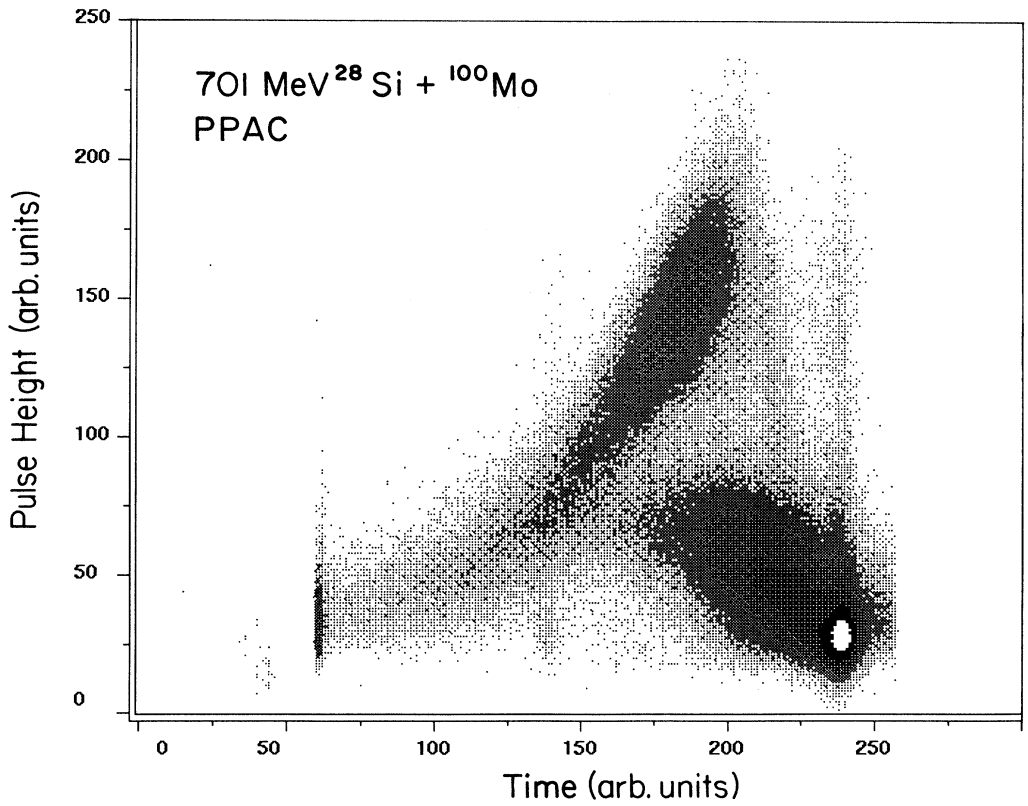

FIG. 1. Two-dimensional map of the PPAC time, relative to the RF pulse, vs PPAC pulse height. The time is determined by a time-to-amplitude converter (TAC) which receives its start from the PPAC and its stop from the cyclotron RF. The intense peak in the lower right-hand corner is due to elastic scattering. The crescent-shaped region is due to fusionlike products. The RF period defines the TAC range, and is 72.9 ns. The FWHM of the elastic peak is 2.9 ns.

which arises from the detection of all the forward light charged particles, takes the form of a Gaussian at the higher velocities. The other one is a background which arises when some forward particle is not detected, as would occur for $\theta_{\rm LCP} < 11°$, resulting in a misidentified channel. This background distribution is peaked at smaller ER velocities, i.e., lower values of the momentum transfers. In order to extract the channel probability, we transform the velocity distributions to a Galilean invariant representation and fit the large $V_{\rm ER}$ portion of the spectra by a Gaussian with an exponential background. The percent yields are listed in the second column in Table I.

A systematic problem with the procedure described above to extract channel yields is that there is no correction for the contribution of the evaporative component in the forward direction. The moving source fits, which are described in detail in Sec. IV, can be used to estimate the magnitude of the underlying evaporative component in the channel definition. We find that at most, 34% of the protons, 24% of the α particles and smaller fractions of the deuterons and tritons selected in the forward Wall can be the result of isotropic evaporation from the residue. In order to reduce the evaporative component in the channel definition, we have obtained distributions similar to those shown in Fig. 2 with the requirement that all particles in the channel definition not only be forward of 35°, but also have energies in excess of the evaporation peak. Fitting of these distributions by the procedure described above produces the relative yields listed in the third column in Table I. While the first procedure, with an unrestricted energy window, overestimates the forward nonevaporative yield, this second procedure probably does the opposite. Therefore, the difference between the two procedures can be used as a measure of the uncertainty of the true nonevaporative channel yield.

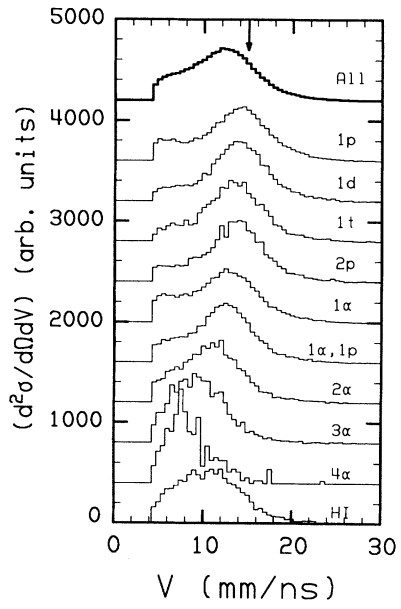

FIG. 2. The channel decomposition of the velocity distribution of fusionlike products. The channels are labeled by the type and number of the forward particles. The top (bold) distribution is the sum of all charged particle channels. The distributions are offset from the abscissa and individually normalized for display. The arrow indicates the velocity expected for full momentum transfer.

A. *Q*-value systematics

The standard picture of incomplete fusion is that of a one-step process, where the channel probabilities are related to the cost of creating the final state. This cost is the sum of the incomplete fusion Q value, $Q_{\rm IF}$, and a Coulomb correction,

$$M_P + M_T \rightarrow M_{ch} + M_R^P + Q_{\rm IF} \ , \tag{1}$$

and

$$Q_{\rm IF}^C = Q_{\rm IF} + (Z_P Z_T - Z_{ch} Z_R^P) e^2 / R_C \ . \tag{2}$$

The masses and charges of the projectile, target, detected channel, and primary residue are given by M_P, M_T, M_{ch}, M_R^P, and Z_P, Z_T, Z_{ch}, and Z_R^P, respectively. The parameter R_C is the distance at which the transfer occurs. The value of R_C is taken as the interaction radius as defined in Ref. 16, which has the value of 11.5 fm for our system. This phenomenological logic has been verified for channels which result in one large projectile remnant. (It has also been used to calculate complete fusion yields.) However, a considerable fraction of the total incomplete fusion yield is in more complicated, highly fragmented channels. To modify Eqs. (1) and (2) to account for these channels, sums must be introduced for the channel properties,

TABLE I. Channel yields.

Channel	Energy integrated (%)	Energy truncated (%)
p	17.4	17.2
d	7.0	11.1
t	4.0	6.8
α	19.7	26.9
$p\ p$	5.1	2.4
$p\ \alpha$	11.4	7.6
$\alpha\ \alpha$	7.1	6.6
$\alpha\ \alpha\ \alpha$	1.6	1.0
$\alpha\ \alpha\ \alpha\ \alpha$	0.2	?
$p\ d$	4.1	3.1
$p\ t$	2.5	2.3
$d\ d$	<0.1	?
$d\ t$	0.9	1.2
$d\ \alpha$	4.8	5.2
$t\ \alpha$	2.7	3.1
$p\ p\ \alpha$	2.9	0.9
$p\ \alpha\ \alpha$	3.5	1.4
$p\ d\ \alpha$	2.4	1.2
$d\ d\ \alpha$	0.5	0.4
$d\ \alpha\ \alpha$	1.4	1.1
$t\ \alpha\ \alpha$	0.8	0.5

$$M_{ch}=\sum_i M_i \ , \tag{3}$$

$$Z_{ch}=\sum_i Z_i \ , \tag{4}$$

where the sums run over all particles in the channel definition.

It is also possible that incomplete fusion proceeds by a two-step process; the first step being a rapid projectile fragmentation followed by the target capturing one or more of the projectile fragments. In this case, the yields might be determined by the cost of the first step. In true projectile fragmentation, when there is no second capturing step, this correlation has been demonstrated by Poulliot *et al.*[17] This cost would be the sum of the projectile fragmentation Q value, $Q_{\rm PF}$, and a Coulomb correction factor. In this case, the Q value is defined by

$$M_P \rightarrow M_{ch}+M_{P-ch}+Q_{\rm PF} \ . \tag{5}$$

The $P-ch$ subscript indicates the remainder of the projectile, which in this scenario ultimately fuses with the target. Since the breakup of the projectile must occur in close proximity to the target, the only new Coulomb term not present on the left-hand side of the equation is that resulting from the interaction between the projectile fragments

$$Q^C_{\rm PF}=Q_{\rm PF}-\tfrac{1}{2}\sum_j\sum_{i\neq j} Z_iZ_je^2/R_P \ . \tag{6}$$

The double sum enumerates all pair interactions amongst the fragments of the projectile. The sum must include not only all fragments in the channel definition but also any piece that is ultimately transferred. We assume that there is only one transferred piece which corresponds to the remainder of the projectile, (Z_P-Z_{ch}). All of these Coulomb interactions result from components of the projectile, so a reasonable choice of the interaction distance is the radius of the projectile, R_P.

These two reaction scenarios, direct incomplete fusion or fusion of some projectile remnant, have different Q values and therefore it is reasonable to compare the correlations between these costs and the channel yields. This is done in Fig. 3. In Figs. 3(a) and 3(b), the yields are plotted as a function of the uncorrected Q value while in Figs. 3(c) and 3(d), the abscissa has been Coulomb corrected. There is little correlation between the uncorrected incomplete fusion Q value [$Q_{\rm IF}$, Fig. 3(a)] and the channel yields. However, the corrected IF Q value [$Q^C_{\rm IF}$, Fig. 3(c)] does correlate quite nicely with the yields. This observation extends the phenomenological basis of the standard incomplete fusion model to highly fragmented channels with large but not complete momentum transfers. This is not meant to imply that incomplete fusion must be a one-step process. In fact, the Q value for projectile fragmentation, with or without correction [Figs. 3(b) and 3(d)] also exhibits a reasonable correlation to the fragment yields.

B. Particle emission characterization

The forward ($\theta_{\rm lab}<35°$) and backward ($\theta_{\rm lab}>35°$) charged particle multiplicities, M_x, as a function of the percentage momentum transfer, ρ, are shown in Figs. 4(a) and 4(b), respectively. (For the purpose of this figure ρ is calculated from the residue velocity assuming that all nonfusing mass moves along the beam direction with the same velocity as the projectile. The fictitious values of $\rho>100\%$ arise from the random nature of the evaporation sequence which can boost $V>V_{\rm full}$.) The open symbols correspond to the inclusive residue-charged particle coincidences while the solid symbols correspond to the specific channels; see below. The trend seen at forward angles, Fig. 4(a), is simply that the more massive the ejectile, the more likely it is to be correlated with slow resi-

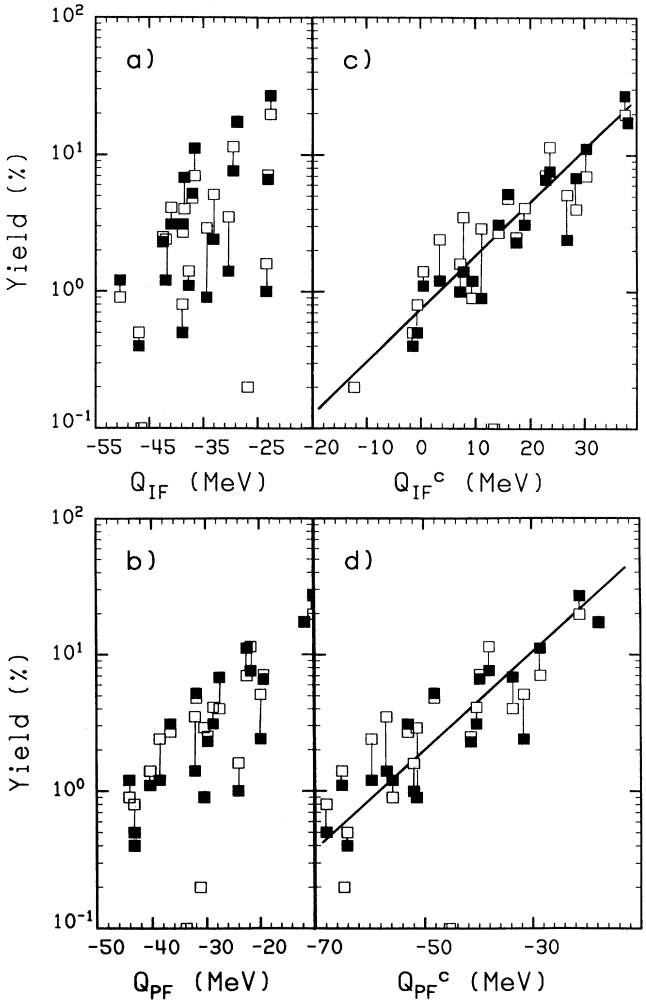

FIG. 3. Correlation between channel probability and Q value. Channels defined by all forward particles regardless of kinetic energy are represented by open squares. Channels defined only by particles with energies in excess of the evaporation peak are represented by solid squares. The corresponding points are connected by a vertical line. The abscissa for (a) is the Q value for incomplete fusion, (b) is the Q value for projectile fragmentation, (c) is the Coulomb corrected Q value for incomplete fusion, and (d) is the Coulomb corrected Q value for projectile fragmentation. The diagonal line is drawn to guide the eye. Table I contains a list of the channels and percentage yields.

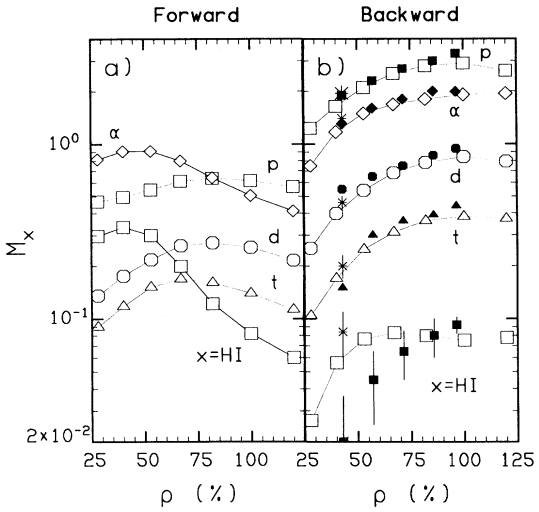

FIG. 4. The multiplicities of charged particles detected at (a) forward ($\theta_{lab} < 35°$) and (b) backward ($\theta_{lab} > 35°$) angles as a function of the linear momentum transfer. The open symbols are derived from inclusive charged particle-residue coincidences. The solid and star symbols are derived from a subset of the inclusive data where specific exclusive channels (forward particles) are selected, see text.

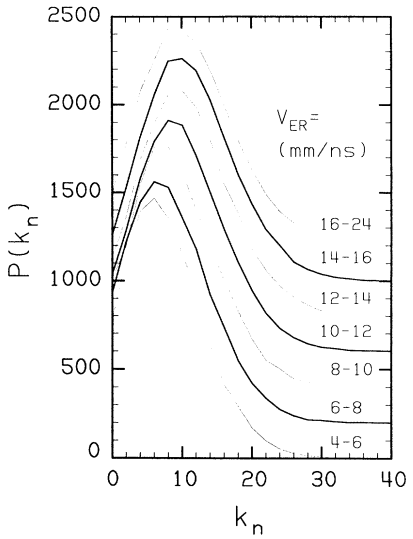

FIG. 5. Neutron fold distributions for seven residue velocity bins. These distributions are deduced from the backward, $\theta_{lab} > 75°$, NaI detectors with an overall solid angle correction to account for the solid angle with $\theta_{lab} < 75°$. The distributions are offset from the abscissa for display. Only NaI detectors at large angles are used because the n/γ-ray discrimination is far superior to that obtained in the forward direction.

dues. This is no more than a verification of the trend seen in Fig. 2.

The inclusive, nonchannel selected light-ion multiplicities in the backward direction [Fig. 4(b)] increase with ρ and tend to saturate as full momentum transfer is approached. The backward angle inclusive heavy-ion multiplicities exhibit a somewhat different trend, saturating at relatively small momentum transfers (slow residues). The dependence observed for the light particles indicates that their multiplicity at large angles is a measure of the violence of the collision in the same fashion as has been previously demonstrated for the neutron multiplicity[18] and as we have also found from the present study (see Fig. 5). Needless to say, the same cannot be said of the forward multiplicities. These reflect the momentum transfer itself, and therefore there is a slight enhancement of $M_{z=1}$ for relatively large values of ρ, while M_α and M_{HI} peak at low values of ρ. The *total* forward charged particle multiplicity is rather insensitive to momentum transfer, and therefore cannot be used as an indicator of the centrality or violence of the collision. This has also been found to be true in the study of the reactions $^{36}Ar+^{238}U$ at $E/A=35$ MeV and $^{14}N+^{238}U$ at $E/A=50$ MeV.[19]

The solid points in Fig. 4(b) are the backward multiplicities (M_p, M_α, M_d, M_t, and M_{HI}) for the specific incomplete fusion channels: $1p$, 1α, 2α, 3α, and 4α with decreasing ρ. At the five values of ρ corresponding to these channels, the solid points represent a subset of data represented by the open points. An additional subset for small ρ is shown by stars which show the backward multiplicities for the forward HI channel with the same momentum transfer as for the 4α channel. For the most part, these channel selected multiplicities agree with each other and the inclusive values. The exceptions are the values of M_{HI} for small ρ. As most of the excitation energy of the fused system is dispensed in the form of neutrons, protons, and α particles, the agreement between the values of M_p and M_α for the channel selected and inclusive data indicates that the value of ρ prescribes a value of the excitation energy.

If the mean excitation energies of the emitting nuclei in the channel selected and inclusive data are the same, and if the backward heavy ions are evaporative emissions from the incompletely fused product, one is led to suspect that angular momentum differences account for the behavior of M_{HI}. Heavy-ion evaporation is known to be far more sensitive to angular momentum than is light particle evaporation.[20] The suppression of M_{HI} for the 3α and 4α channels (the solid squares near the bottom of the figure at $\rho=57\%$ and 43%, respectively) implies that the transferred spin for these channels must be less than the transferred spin for other channels contributing to the same region of ρ. If this is so, the opposite must be true of the HI channel, stars in Fig. 4. While the total excitation energy is virtually the same as the 4α channel and the inclusive data (see M_p and M_α), the M_{HI} in the heavy-ion channel (stars) is significantly larger than that arising from the 4α channel. This suggests that the highly fragmented incomplete fusion channels transfer less angular momentum than does the channel with an intact spectator.

The influence of angular momentum might also provide an explanation for the overall dependence of M_{HI} on momentum transfer. As pointed out earlier, M_{HI} increases faster at low ρ and saturates sooner than do the

light-ion multiplicities. This can be understood if the angular momentum transferred to the fusion product decreases with ρ for the events seen in this study, those producing residues near 0°. The heavy-ion emission is sensitive to both excitation energy and spin and therefore M_{HI} would not increase with excitation energy if the spin is decreasing. On the other hand, light-ion evaporation simply reflects the increase in excitation energy which is strictly increasing with increasing ρ.

It is also possible that the channel dependence of the yield of backward angle heavy ions is due to a true dynamical correlation between forward projectilelike fragments and projectile remnants which have orbited to large angles. In fact, the dynamical α-cluster model of Möhring *et al.*[21] does predict the correlation that we observe, fewer α clusters (HI) when the forward spray of particles is highly fragmented. This model[21] allows the projectile, treated as a cluster of α particles, to break up into individual α particles or smaller α clusters. These α particles or clusters can proceed forward thus composing an incomplete fusion channel, orbit and be ejected at large angles or fuse.

It is possible that this dynamical process can be distinguished from the statistical angular momentum driven explanation, using the angular distributions. However, the present experiment has insufficient statistics to generate meaningful channel gated heavy-ion angular distributions.

IV. MOMENTUM RECONSTRUCTION AND EXCITATION ENERGY DETERMINATION

While the initial dynamics of these reactions is complex, at some time the fusion product evolves into a hot compound nucleus which decays as determined by the statistical properties of the entire remaining system. However, there are important unanswered questions concerning the statistical decay of highly excited nuclei. How does the prescription for calculating the level density evolve with excitation energy? What role is played by large-fragment emission or other exotic decay modes? Is there an upper limit in the temperature which describes the statistical properties of the highly excited system? We are therefore interested not only in the fast noncompound reaction steps, but also in the properties of the highly excited fusion product. In this section, we present a momentum reconstruction, which provides some insight into the relative importance of the various possible fast mechanisms, and an excitation energy reconstruction of the compoundlike object, which is useful for the study of the questions posed above.

We know from examining Fig. 2 that we do not detect the complete momentum that of the beam. When a forward going particle escapes detection, the channel is misidentified and the residue velocity is too low to be consistent with the identified channel. The missing momentum is therefore correlated with slow residues. Since our detection is blind to projectile fragments for $\theta_{\mathrm{lab}} < 11°$, most of the missing momentum must be directed at these angles and is likely to be in the form of fast beamlike particles. Taking this into account, we have adopted the following procedure to determine the partition of momentum and ultimate excitation of the compoundlike object.

The data are divided into seven bins based on cuts in the velocity of the residue. The mean velocities of these bins range from 28%, Bin No. 1, to over 100%, Bin No. 7, of the value expected for full momentum transfer. (Residue velocities greater than 100% of the value for full momentum transfer are expected due to recoil effects.) Neutron fold distributions were generated for each bin from the backward angle data by applying a solid angle correction, see Fig. 5. The average neutron multiplicity M_n is deduced from the average fold.[14] Since these multiplicities are deduced from backward angle data ($\theta_{\mathrm{lab}} < 75°$) they are associated with the decay of the compoundlike object. The binned charged particle spectra are fitted to a composite source model. Three sources are included: one to mock up projectile fragmentation (P like), another to include a fast, preequilibrium emission of particles (int), and a third source for the compoundlike evaporation (ev). The first and the third of these sources are modeled by a Coulomb shifted surface Maxwellian, boosted into the laboratory frame by the appropriate velocity. The intermediate velocity source was modeled by the standard moving source parametrization,[22] which postulates a source moving along the beam direction and experiencing a Coulomb repulsion from a spectator stationary in the laboratory. Representative spectra and the composite source model fits are shown in Figs. 6–8 for protons, deuterons, and α particles, respectively. The fits provide an excellent representation of the spectra of all particles at all angles from energies near the barrier on up. The multiplicities and temperatures deduced from the fits are plotted in Figs. 9 and 10 as a function of residue velocity, and listed along with the other parameters associated with these fits in Table II. The errors given in parentheses in Table II are the statistical errors from the fitting procedure. The deuteron and triton multiplicities have an additional systematic uncertainty arising from the fact that the loci for these particles in the raw data maps merge with that for protons at very low energy. We estimate that this problem could result in at most a 25% underestimate of these multiplicities. The multiplicities and temperature parameters extracted from the three-component fits exhibit the same trends as seen in Fig. 4. The evaporative multiplicities (solid squares) increase with residue velocity or momentum transfer as do the ratios $M^d_{\mathrm{ev}}/M^p_{\mathrm{ev}}$ and $M^t_{\mathrm{ev}}/M^p_{\mathrm{ev}}$ (not shown). The projectilelike (triangles) and intermediate (circles) multiplicities reflect the momentum transfer itself, the heavier the particle, the greater the association with the slower residue velocities. The temperature parameters for the evaporative component (squares in Fig. 10) also increase monotonically with momentum transfer from 3.5 MeV to slightly over 5 MeV. There is no clear evidence of a saturation of T^i_{ev} over this range. The values of T^{α}_{ev} are slightly greater than T^p_{ev}. This difference is to a large extent due to the influence of angular momentum. This point is discussed at some length in the accompanying paper.[13] The temperature parameters for the relatively weak projectilelike component (see multiplicities in Fig.

9, triangles in both Figs. 9 and 10) are generally smaller than those for the evaporative component. On the other hand, the temperature parameters for the intermediate source are larger and increase with momentum transfer. These intermediate source temperature parameters are so large that if such a source really existed with such a temperature, it would completely decompose. The physical interpretation of this parameter is not clear. However, the need of a large slope parameter for the intermediate source in multisource fits such as the ones one in this work is well documented (for example, see Ref. 23).

This multiple source picture is undoubtedly a great simplification of the true reaction dynamics. As mentioned before, it is designed only to allow us to keep account of the momenta and to deduce the excitation energy of the compound system. The operational definition of the compound system is determined by the source construction and is therefore the system which deexcites by the emission of particles which exhibit a forward-backward symmetry in the rest frame moving with the velocity of the ultimate residue. The procedure we use for this is, with one exception, identical to the procedure used by Wada *et al.*[23] A residue velocity is calculated using the momentum and mass associated with the first two sources, projectilelike and preequilibrium. If this velocity differs from the experimental one (which it does for the lower velocity bins) an additional momentum in the form of the projectilelike source is included to correct this discrepancy. With this consistency, an excitation energy at the beginning of the evaporation stage can be calculated using the initial momentum transfer, the result of the first step, and then subtracting the cost of the preequilibrium emissions. This "top-down" procedure does not directly use the parameters from the evaporation source

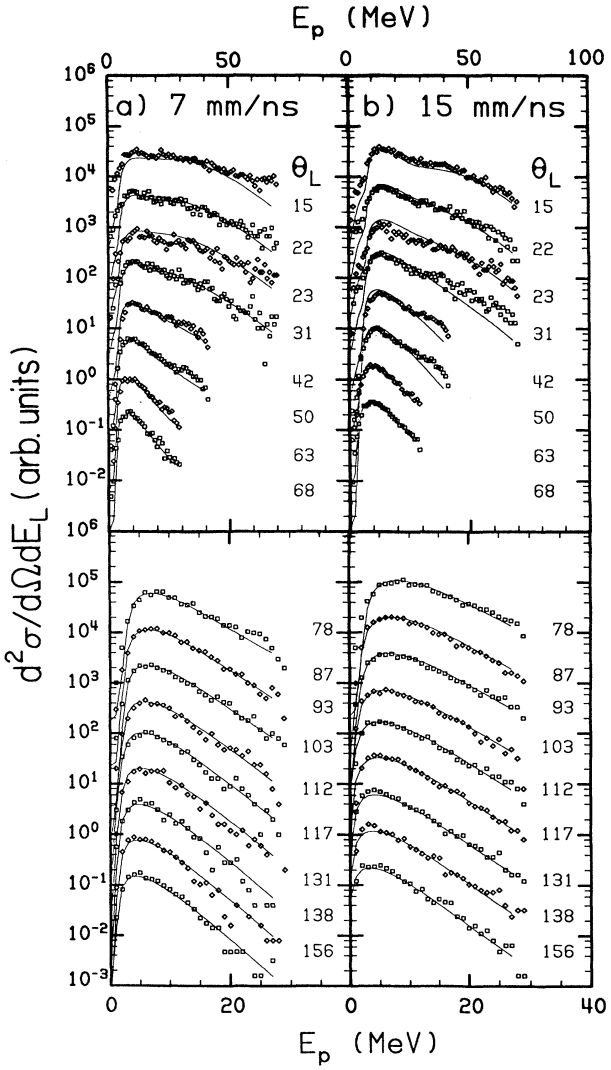

FIG. 6. Proton spectra for two selected bins of the residue velocity: (a) 7 mm/ns and (b) 15 mm/ns. The laboratory angles are indicated. The lines are the fits described in the text.

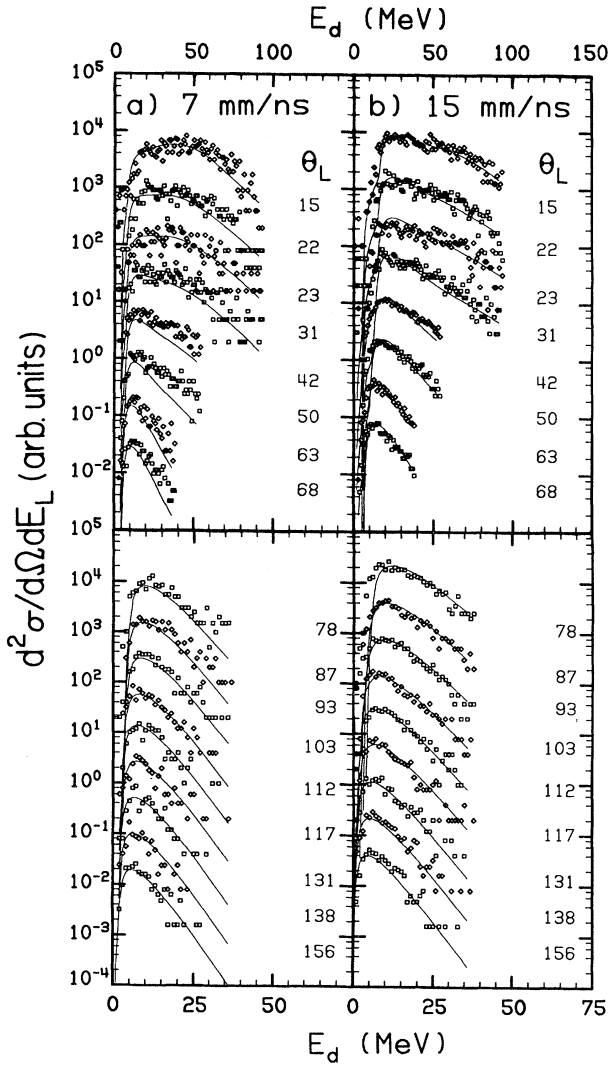

FIG. 7. Deuteron spectra for two selected bins of the residue velocity: (a) 7 mm/ns and (b) 15 mm/ns. The laboratory angles are indicated. The lines are the fits described in the text.

or the neutron multiplicities or the sum γ-ray energies. Therefore the top-down excitation is checked against a "bottom-up" excitation energy determination using these other data.

More formally, this logic is as follows. (The reader may also refer to Ref. 23.) In the first step, the projectile breaks up, some of it fuses and the remainder escapes. Of the escaping component, some fraction of the momentum is detected $P_{P\ \mathrm{like}}$ and the remainder avoids detection, ΔP. The fractional momentum transfer, ρ_1 (relative to that of the projectile, P_p) at this stage is

$$\rho_1 = 1 - \left[\frac{\sum_i M^i_{P\ \mathrm{like}} A^i V^i_{P\ \mathrm{like}}\ \Delta P}{P_p} \right] . \tag{7}$$

The sum index extends over all charged particles with mass A^i and neutrons. See below for the details concerning the neutron parameters. The fitted values of the velocity ($V_{P\ \mathrm{like}} = 93-100\%$ of V_{proj}, see Table II) and the multiplicity ($M^i_{P\ \mathrm{like}}$) for the projectilelike source are used in (7). The excitation at this stage is

$$E^*_1 = \frac{A_T E_P}{A_P + (A_T/\rho_1)} + Q_1 , \tag{8}$$

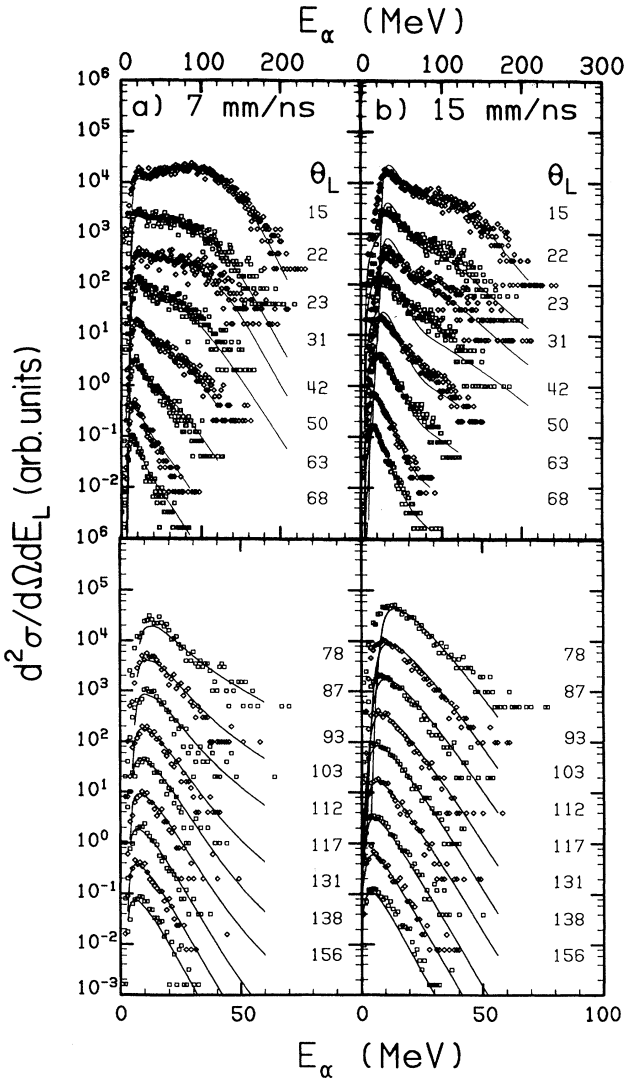

FIG. 8. α particle spectra for two selected bins of the residue velocity: (a) 7 mm/ns and (b) 15 mm/ns. The laboratory angles are indicated. The lines are the fits described in the text.

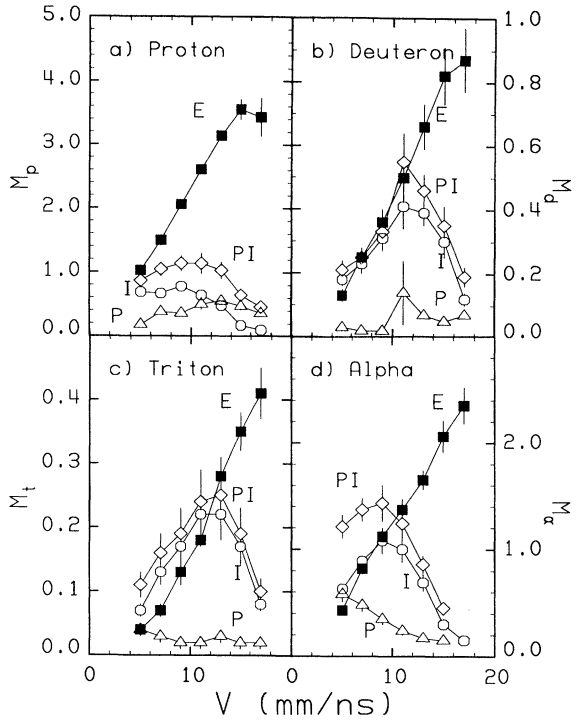

FIG. 9. Proton (a), deuteron (b), triton (c), and α-particle (d) multiplicities extracted from the three source fit to the experimental data. The data and fits are shown in Figs. 6–8. Triangles are used for $M^i_{P\ \mathrm{like}}$, circles for M^i_{int}, diamonds for $M^i_{P\ \mathrm{like}} + M^i_{\mathrm{int}}$, and solid squares for M^i_{ev}.

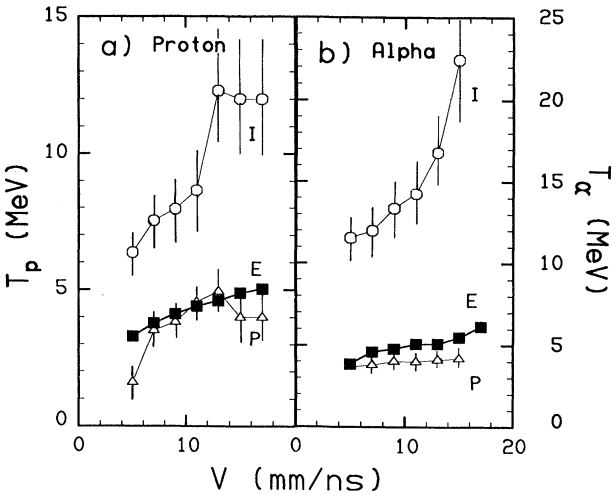

FIG. 10. Proton (a) and α-particle (b) temperatures extracted from the three source fit to the experimental data. The data and fits are shown in Figs. 6–8. The symbols represent the same components as they did in Fig. 9.

TABLE II. Extracted parameters from the fitted *p*, *d*, *t*, and α spectra using three Maxwellian sources.

Particle	Source[a]	V_S[b] (mm/ns)	M[c]	T[d] (MeV)	Cb[e] (MeV)	ϵ[f] (MeV)	$M[(BE)+\epsilon]$[g] (MeV)
Bin no. 1							
p	ev	5.0	1.03(0.06)	3.29(0.08)	3.7(0.4)	10.3	14.3
d	ev	5.0	0.13(0.02)	3.73(0.17)	5.2(0.8)	13.5	3.2
t	ev	5.0	0.04(0.01)	4.00(0.17)	4.2(0.5)	12.4	1.2
α	ev	5.0	0.43(0.04)	3.87(0.12)	7.8(1.0)	15.5	6.4
n	ev	5.0	8.02(0.80)	3.29(0.08)		6.6	136.8
HI	ev	5.0	0.03(0.01)	3.87(0.12)	11.7(2.0)	19.4	0.6
p	int	52.0	0.69(0.07)	6.36(1.0)	7.5(1.2)		
d	int	54.0	0.18(0.02)	6.36(1.0)	5.2(1.0)		
t	int	42.0	0.07(0.01)	6.36(1.0)	5.2(1.0)		
α	int	35.0	0.63(0.04)	11.6(1.5)	7.0(1.2)		
p	*P* like	69.0	0.18(0.02)	1.60(0.6)	1.0(3.0)		
d	*P* like	64.0	0.03(0.01)	3.60(0.5)	1.0(3.0)		
t	*P* like	64.0	0.04(0.01)	4.00(0.7)	1.0(3.0)		
α	*P* like	67.0	0.58(0.07)	3.69(0.5)	1.4(3.0)		
Bin No. 2							
p	ev	7.0	1.50(0.08)	3.78(0.10)	3.5(0.3)	11.0	22.0
d	ev	7.0	0.25(0.02)	4.12(0.11)	5.4(1.0)	14.7	6.5
t	ev	7.0	0.07(0.01)	4.20(0.20)	5.4(1.0)	14.7	2.2
α	ev	7.0	0.82(0.05)	4.61(0.10)	7.6(1.2)	16.8	13.2
n	ev	7.0	8.64(0.86)	3.78(0.10)		7.6	156.0
HI	ev	7.0	0.06(0.02)	4.61(0.10)	11.3(2.0)	20.6	1.2
p	int	51.0	0.67(0.07)	7.53(1.2)	7.8(1.3)		
d	int	49.0	0.23(0.03)	7.53(1.2)	5.4(1.0)		
t	int	42.0	0.13(0.02)	7.53(1.2)	5.4(1.0)		
α	int	35.0	0.89(0.05)	12.0(1.7)	6.9(1.2)		
p	*P* like	65.0	0.38(0.04)	3.51(0.06)	1.0(3.0)		
d	*P* like	65.0	0.02(0.01)	1.57(0.5)	1.0(3.0)		
t	*P* like	65.0	0.03(0.01)	2.05(0.7)	1.0(3.0)		
α	*P* like	68.0	0.48(0.06)	3.80(0.4)	2.1(3.0)		
Bin No. 3							
p	ev	9.0	2.06(0.07)	4.12(0.07)	3.4(0.4)	11.6	31.3
d	ev	9.0	0.36(0.03)	4.54(0.16)	5.7(1.0)	15.1	9.6
t	ev	9.0	0.13(0.02)	4.90(0.20)	3.9(1.5)	17.3	4.0
α	ev	9.0	1.12(0.08)	4.81(0.12)	8.0(1.4)	17.6	19.0
n	ev	9.0	9.28(0.93)	4.12(0.07)		8.2	174.0
HI	ev	9.0	0.08(0.02)	4.81(0.12)	12.0(2.0)	21.6	1.7
p	int	50.0	0.78(0.08)	7.96(1.3)	9.5(2.0)		
d	int	50.0	0.31(0.04)	7.96(1.3)	5.7(1.0)		
t	int	45.0	0.17(0.03)	7.96(1.3)	3.9(1.5)		
α	int	35.0	1.08(0.12)	13.4(1.7)	4.8(1.0)		
p	*P* like	65.0	0.36(0.04)	3.82(0.6)	1.0(3.0)		
d	*P* like	65.0	0.02(0.01)	2.00(0.7)	1.0(3.0)		
t	*P* like	65.0	0.02(0.01)	4.00(1.0)	1.0(3.0)		
α	*P* like	67.0	0.35(0.05)	4.03(0.4)	4.8(1.5)		
Bin No. 4							
p	ev	11.0	2.61(0.06)	4.40(0.07)	3.4(0.6)	12.2	41.2
d	ev	11.0	0.50(0.03)	4.60(0.10)	6.4(1.2)	16.2	13.8
t	ev	11.0	0.18(0.01)	5.00(0.20)	4.2(1.5)	17.2	5.9
α	ev	11.0	1.37(0.10)	5.00(0.10)	8.2(1.6)	18.4	24.2
n	ev	11.0	10.2(1.0)	4.40(0.07)		8.8	197.0
HI	ev	11.0	0.08(0.02)	5.00(0.10)	12.3(1.8)	22.5	1.8

TABLE II. (*Continued*).

Particle	Source[a]	V_S[b] (mm/ns)	M[c]	T[d] (MeV)	Cb[e] (MeV)	ϵ[f] (MeV)	$M[(BE)+\epsilon]$[g] (MeV)
p	int	46.0	0.64(0.08)	8.65(1.8)	10.8(1.5)		
d	int	50.0	0.41(0.07)	8.65(1.8)	6.3(1.2)		
t	int	47.0	0.22(0.04)	8.65(1.8)	4.2(1.0)		
α	int	35.0	1.00(0.12)	14.3(2.0)	4.8(1.0)		
p	P like	69.0	0.50(0.08)	4.55(0.6)	1.0(3.0)		
d	P like	69.0	0.14(0.20)	2.10(0.7)	1.0(3.0)		
t	P like	69.0	0.02(0.01)	4.00(0.4)	1.0(3.0)		
α	P like	67.0	0.24(0.04)	4.00(0.4)	3.4(1.5)		
Bin No. 5							
p	ev	13.0	3.14(0.08)	4.60(0.10)	3.6(0.6)	12.8	51.5
d	ev	13.0	0.66(0.04)	5.08(0.14)	6.2(1.1)	17.3	19.0
t	ev	13.0	0.28(0.03)	5.50(0.16)	3.5(1.0)	17.5	9.3
α	ev	13.0	1.65(0.09)	5.11(0.10)	9.3(1.8)	19.5	31.0
n	ev	13.0	10.9(1.1)	4.60(0.10)		9.2	215.0
HI	ev	13.0	0.08(0.02)	5.11(0.10)	14.0(2.0)	24.2	1.9
p	int	56.0	0.48(0.06)	12.3(2.2)	5.4(0.8)		
d	int	47.0	0.39(0.04)	12.3(2.2)	6.2(1.2)		
t	int	46.0	0.22(0.04)	12.3(2.2)	3.5(1.0)		
α	int	35.0	0.69(0.08)	16.8(2.2)	4.9(0.6)		
p	P like	66.0	0.55(0.07)	4.93(0.7)	1.0(3.0)		
d	P like	66.0	0.07(0.01)	3.00(0.8)	1.0(3.0)		
t	P like	66.0	0.03(0.01)	4.00(0.8)	1.0(3.0)		
α	P like	66.0	0.17(0.03)	4.12(0.3)	3.4(1.5)		
Bin No. 6							
p	ev	15.0	3.55(0.16)	4.88(0.10)	3.6(0.5)	13.5	60.3
d	ev	15.0	0.82(0.05)	5.60(0.14)	7.1(1.3)	18.4	24.5
t	ev	15.0	0.35(0.03)	6.80(0.20)	4.4(1.5)	19.8	12.4
α	ev	15.0	2.06(0.15)	5.50(0.12)	10.1(1.7)	21.0	42.0
n	ev	15.0	11.3(1.2)	4.88(0.10)		9.8	229.0
HI	ev	15.0	0.08(0.02)	5.50(0.12)	15.1	26.1	2.1
p	int	40.0	0.17(0.03)	12.0(2.3)	3.8(0.5)		
d	int	50.0	0.30(0.05)	12.0(2.3)	7.1(2.5)		
t	int	45.0	0.17(0.03)	12.0(2.3)	4.4(1.0)		
α	int	38.0	0.30(0.05)	22.4(4.0)	3.8(0.5)		
p	P like	69.0	0.47(0.06)	4.00(0.8)	1.2(3.0)		
d	P like	69.0	0.05(0.01)	2.68(0.6)	1.0(3.0)		
t	P like	69.0	0.02(0.01)	4.00(0.8)	1.0(3.0)		
α	P like	67.0	0.15(0.02)	4.20(0.4)	1.0(3.0)		
Bin No. 7							
p	ev	17.0	3.43(0.30)	5.03(0.15)	3.4(0.5)	13.9	59.8
d	ev	17.0	0.87(0.05)	6.08(0.23)	7.4(1.4)	19.6	27.0
t	ev	17.0	0.41(0.04)	7.47(0.50)	4.9(1.5)	19.8	14.5
α	ev	17.0	2.35(0.17)	6.15(0.35)	10.0(1.7)	22.3	50.7
n	ev	17.0	11.2(1.2)	5.03(0.15)		10.1	231.0
HI	ev	17.0	0.08(0.02)	6.15(0.35)	15.0(2.5)	27.3	2.2
p	int	40.0	0.10(0.02)	12.0(2.3)	1.0(3.0)		
d	int	42.0	0.12(0.02)	12.0(2.3)	7.4(2.0)		
t	int	44.0	0.08(0.01)	12.0(2.3)	4.9(1.0)		
α	int	59.0	0.15(0.02)	6.08(2.0)	14.7(4.0)		

TABLE II. (*Continued*).

Particle	Source[a]	V_S[b] (mm/ns)	M[c]	T[d] (MeV)	Cb[e] (MeV)	ϵ[f] (MeV)	$M[(\mathrm{BE})+\epsilon]$[g] (MeV)
p	P like	69.0	0.36(0.05)	4.00(0.8)	1.5(2.0)		
d	P like	69.0	0.07(0.01)	4.00(0.8)	7.4(2.0)		
t	P like	69.0	0.02(0.01)	4.00(0.8)	1.0(3.0)		
α	P like						

[a]The sources: (ev) is the evaporative, (int) is the intermediate and (P like) is the projectilelike.
[b]The source velocity. The velocity of the evaporative source was fixed at the centroid of the residue velocity window. The velocities are fitted for the other two sources.
[c]The multiplicity. Neutron and heavy-ion multiplicities are deduced from the backward angle event by event data.
[d]The temperature parameters deduced from the fitted spectra. Neutron and heavy-ion temperatures were assumed equal to the proton and α temperatures, respectively.
[e]The Coulomb barrier. $(\mathrm{Cb})^{\mathrm{HI}}$ was assumed equal to $1.5(\mathrm{Cb})^{\alpha}$.
[f]The average kinetic energy.
[g]Excitation energy removed. (BE) is the binding energy.

where E_P is the total laboratory energy and A_P and A_T are the mass numbers of the projectile and target. The Q value for this step is that for the entire incomplete fusion reaction. One can envision correcting Q_1 with a Coulomb term which would provide some energy for the escaping projectilelike fragments to break up. However, we see no obvious way to make this undoubtedly small correction so we simply use $Q_1 = Q_{\mathrm{IF}}$, Eq. (1). After this incomplete fusion stage, the mass and velocity of the system are,

$$A_1 = A_P + A_T - \sum_i M^i_{P\ \mathrm{like}} A^i - \Delta A \tag{9}$$

and

$$v_1 = \rho_1 P_p / A_1 \ . \tag{10}$$

The missing mass ΔA is deduced from the missing momentum assuming $\Delta P = \Delta A\,(P_p / A_p)$.

The next step in the reaction is a fast preequilibrium emission of particles. This intermediate source has a velocity, v_{int}, approximately $\frac{1}{2}$ that of the beam, see Table II. From the parameters of the fit of this component, the residue velocity V_R, mass A^P_R, and excitation energy $E^*_{R,\mathrm{down}}$ can be calculated by subtracting the appropriate terms from v_1, A_1, and E^*_1,

$$V_R = \frac{A_1 v_1 - \sum_i M^i_{\mathrm{int}} A^i v^i_{\mathrm{int}}}{A_1 - \sum_i M^i_{\mathrm{int}} A^i} \ , \tag{11}$$

$$A^P_R = A_1 - \sum_i M^i_{\mathrm{int}} A^i \ , \tag{12}$$

$$E^*_{R,\mathrm{down}} = E^*_1 - \sum_i [M^i_{\mathrm{int}} (B^i_{\mathrm{int}} + \tfrac{3}{2} T^i_{\mathrm{int}})] + Q_2 \ . \tag{13}$$

The intermediate source parameters of multiplicity, velocity, Coulomb barrier, and temperature for the channels, (n, p, d, t, and α particles) are indicated by M^i_{int}, v^i_{int}, B^i_{int}, and T^i_{int}, respectively. The Q value for Eq. (13) is the energy required to separate A_1 into the intermediate source components and the ultimate residue

$$A_1 \rightarrow A^P_R + \sum_i M^i_{\mathrm{int}} A^i + Q_2 \ . \tag{14}$$

[Equation (13) differs from the expression used by Wada *et al.*[23] They neglected the Coulomb term and explicitly included a recoil correction. The recoil term is much smaller than the Coulomb term, which itself is small. We neglect the smaller recoil term.]

The number of preequilibrium neutrons is assumed to be independent of ρ_1 and equal to 2.5, this value is that determined by Hilscher[18] for the system $^{20}\mathrm{Ne}+^{165}\mathrm{Ho}$ at 30 MeV/A. We assume that the fractional partition of neutrons between the projectilelike and intermediate sources is the same as for protons and that the neutron source velocities are the same as the proton source velocities.

The results of this analysis are also given in Table III and plotted in Figs. 11–13. The mass and linear momentum partition are shown in Figs. 11 and 12, respectively. The mass of the primary residue A^P_R (solid squares in Fig. 11) increases from 105 amu for the lowest momentum transfers to 122 amu for the bins near complete momentum transfer. The balance of the mass is found in the intermediate source (triangles in Fig. 11) which contains as many as 10 nucleons, the projectilelike source (circles) with as many as four nucleons, and the unobserved or missing mass (open squares) with as many as 10 nucleons. As discussed previously, these nonevaporative sources are concentrated at low momentum transfers. It is worth noting that the three bins with the largest momentum transfer require no missing mass and the next, fourth bin, only requires two unaccounted-for nucleons. The influence of the fast intermediate, projectilelike, and missing components is highlighted in the momentum reconstruction, Fig. 12.

The excitation energy of the primary residue for each bin is shown in Fig. 13. The open squares are the excitation energies determined from the momentum reconstruction procedure, $E^*_{R,\mathrm{down}}$ from Eq. (13). The solid squares are calculated from the multiplicities and channel energies of the evaporative component ϵ^i and the total γ-ray energy,

TABLE III. Linear momentum partition and excitation energy reconstruction.

	Linear momentum partition.										
Bin	$P_{P\ \mathrm{like}}/P_i$[a]	P_{int}/P_i[b]	$M_{P\ \mathrm{like}}$	M_{int}	M_{ev}	ρ_1	$\Delta P/P_i$[c]	ΔA	A_1	A_R^P	A_R
1	0.151	0.154	4.32	7.05	9.82	0.849	0.422	11.82	112	105	95
2	0.150	0.174	4.30	8.43	12.41	0.850	0.304	8.52	115	107	94
3	0.110	0.200	3.22	9.72	14.56	0.890	0.192	5.38	119	110	95
4	0.105	0.179	2.97	8.72	16.48	0.895	0.086	2.40	123	114	97
5	0.102	0.143	2.93	6.50	18.32	0.900	0.000	0.00	125	119	100
6	0.114	0.075	3.21	3.53	20.34	0.900	0.000	0.00	125	121	101
7	0.113	0.052	3.20	2.57	21.42	0.900	0.000	0.00	125	122	101

	Excitation energy reconstruction					
Bin	E_1^* (MeV)	$E_{R,\mathrm{down}}^*$ (MeV)	$E_{R,\mathrm{up}}^*$ (MeV)	$E_{R,\mathrm{down}}^*/A_R^P$ (MeV/A)	$E_{R,\mathrm{up}}^*/A_R^P$ (MeV/A)	$\Delta E/E$[d] (%)
1	242	158	174	1.50	1.66	−10.3
2	290	200	212	1.87	1.99	−6.4
3	368	260	251	2.37	2.29	3.4
4	413	316	295	2.77	2.59	6.6
5	463	372	339	3.14	2.86	8.9
6	458	405	381	3.34	3.14	6.0
7	458	418	396	3.42	3.24	5.4

[a]Contribution of the projectilelike source momentum, P_i is the projectile linear momentum.
[b]Contribution of the intermediate source momentum.
[c]Contribution of the missing momentum.
[d]The relative error between $E_{R,\mathrm{down}}^*$ and $E_{R,\mathrm{up}}^*$. The other parameters are defined in text.

$$E_{R,\mathrm{up}}^* = E_{\mathrm{total}}^{\gamma} + \sum_i M_{\mathrm{ev}}^i [\epsilon^i + (BE)^i] \ . \tag{15}$$

The sum extends over n, p, d, t, α, and heavy ions. The mean neutron energy ϵ^n is taken as that of the proton less the proton barrier. Experimental masses are used to calculate the binding energies, $(BE)^i$. The contributions of the various terms in Eq. (15) are given in the last column in Table II. The total γ-ray energy, $E_{\mathrm{total}}^{\gamma}$ is close to 10 MeV for all of the bins. We have also found that M_{γ} is independent of momentum transfer. The lack of the latter dependence can be understood with the aid of statistical model calculations which indicate that only a small portion of the spin is removed by γ rays. We also

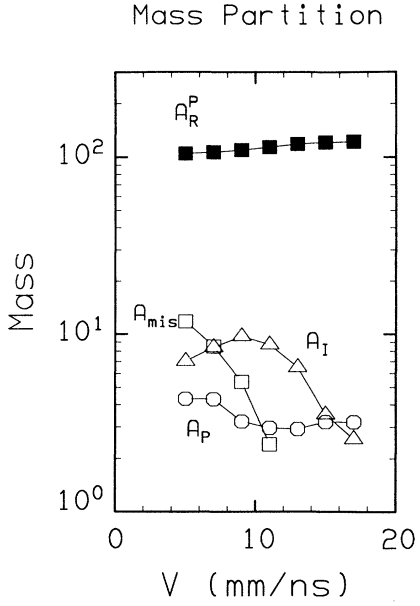

FIG. 11. Mass partition. The circles give the projectilelike mass, A_P; triangles, the intermediate source; open squares, the undetected mass; and solid squares, the initial mass of the compound system.

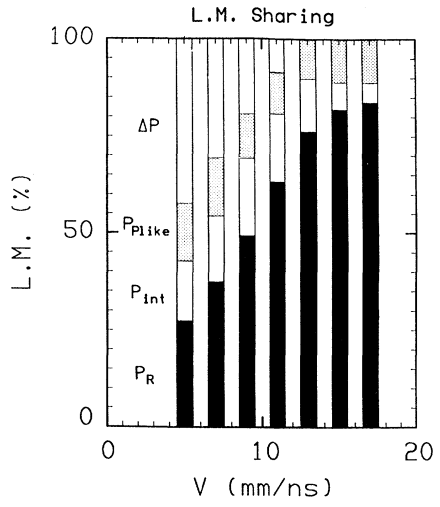

FIG. 12. Histogram displaying the partition of linear momentum between the residue, P_R, the intermediate source, P_{int}, the projectilelike source, $P_{P\ \mathrm{like}}$, and the missing momentum ΔP.

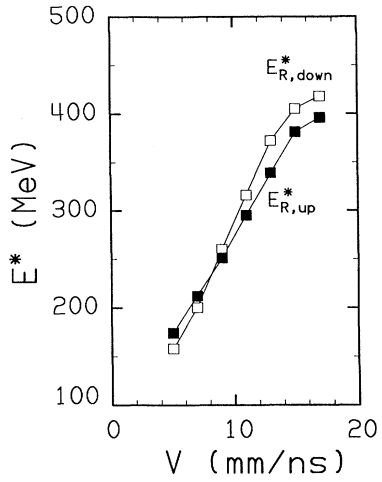

FIG. 13. The initial compound excitation energy, as determined by the "top-down" momentum reconstruction (solid squares) and the excitation deduced from summing the particle emission costs from the "bottom up" (open squares), plotted as a function of residue velocity.

find that even at the highest excitation energy, over 400 MeV, heavy-ion evaporation makes a negligible contribution to the deexcitation mechanism.

The comparison of $E^*_{R,\mathrm{down}}$ (open squares) and $E^*_{R,\mathrm{up}}$ (solid squares) presented in Fig. 13, provides confidence that the mean initial compound excitation energies have been determined reasonably well. The disagreement between the two methods is less than 10% over the entire span covering E^*_R from 170 to 420 MeV, (see Table III for the numbers). The terms contributing the most to the uncertainty in the determination of E^*_R from either direction have to do with the neutron parameters. For the determination of $E^*_{R,\mathrm{down}}$, it is the total number of preequilibrium neutrons and how they are distributed in energy and angle, which creates the greatest uncertainty. As stated previously, we assume that these neutrons can be modeled by the sum of a projectilelike component and an intermediate velocity source in the same fashion as protons with an overall multiplicity taken from the literature for a similar system. While these are reasonable assumptions, we cannot verify them with the existing data. For the determination of $E^*_{R,\mathrm{up}}$, the primary source of uncertainty is the multiplicity of evaporation neutrons. While this is determined in our experiment, it is done with a device (Spin Spectrometer) not ideally suited to the task. We estimate that the absolute uncertainty in M^n_{ev} is less than 20%. This propagates into a 12–15 % uncertainty in $E^*_{R,\mathrm{up}}$. This agreement between the two methods suggests that the uncertainty in E^*_R is no more than this. Some additional verification of these excitation energies could be achieved in an experiment with individual mass identification of the ultimate residue, A_R. In this case, the final product of the decay of the primary residue with mass A^P_R and excitation energy E^*_R can be compared to statistical model calculations.

V. SUMMARY AND CONCLUSIONS

This work is a rather complete study of the reactions between 701 MeV ^{28}Si and ^{100}Mo which produce a residue near 0°. These reactions are incomplete fusions. We have found that the yields correlate with the Coulomb corrected Q values corresponding to either the entire incomplete fusion reaction or the simple projectile fragmentation. This means that we cannot learn about the nature of the mechanism from the Q-value yield systematics alone. On the other hand, we do know that a Coulomb correction must be applied, even for the highly fragmented channels considered here, in order to make the incomplete fusion systematics work.

We have also learned that there is a difference in the dependence of light- and heavy-ion multiplicities with linear momentum transfer. Related to this, we have seen that the backward angle heavy-ion multiplicities depend on the extent of fragmentation while the light-ion multiplicities do not. This can be explained within the framework of equilibrium evaporation if there is a systematic difference in the transferred spin distributions with the extent of fragmentation, at fixed linear momentum transfer. However, at least one dynamical explanation also exists.

The data from this experiment has been used to determine the partition of the mass and momentum and the deposition of excitation energy. These reactions produce highly excited nuclei. While these nuclei are not as well characterized as simple compound reactions, they are sufficiently well characterized to allow detailed studies of the decay of these systems. One of the central issues is the development of the nuclear level density at these high excitation energies. This is dealt with in the following paper.

ACKNOWLEDGMENTS

This work was supported in part by the U.S. Department of Energy under Contract Nos. DE-FG02-87ER40316 and DE-FG02-88ER40406. Oak Ridge National laboratory is operated by Martin Marietta Energy Systems, Inc. under Contract No. DE-AC05-84OR21400 with the U.S. Department of Energy.

*Permanent address: Institute of Physics, Jagellonian University of Kraków, Kraków, Poland.

†Permanent address: Wadsworth Center for Laboratories and Research, New York State Department of Health, Albany, NY 12201.

[1]H. Morgenstern, W. Bohne, W. Galster, K. Grabisch, and A. Kyanowski, Phys. Rev. Lett. **52**, 1104 (1984); Y. Chan, C. Albiston, M. Bantel, A. Budzanowski, D. DiGregorio, R. G. Stokstad, S. Wald, S. Zhou, and Z. Zhou, *Proceedings of the Symposium on the Many Facets of Heavy-Ion Fusion Reactions,* Argonne, 1986 (Argonne National Laboratory Report ANL-PHY-86-01, 1986), p. 219.

[2]K. Kwiatkowski, Nucl. Phys. **471**, 271c (1987).
[3]J. Wilczyński, K. Siwek-Wilczyńska, J. Van Driel, S. Gonggrijp, D. C. J. M. Hageman, R. V. F. Janssens, J. Lukasiak, and R. H. Siemssen, Phys. Rev. Lett. **45**, 606 (1980); J. Wilczyński, K. Siwek-Wilczyńska, J. Van Driel, S. Gonggrijp, D. C. J. M. Hageman, R. V. F. Janssens, J. Lukasiak, R. H. Siemssen, and S. Y. Van Der Werf, Nucl. Phys. **A373**, 109 (1982).
[4]J. P. Bondorf, J. N. De, G. Fai, A. O. T. Karvinen, B. Jakobsson, and J. Randrup, Nucl. Phys. **A333**, 285 (1980).
[5]K. Möhring, W. J. Swiatecki, and M. Zielińska-Pfabé, Nucl. Phys. **A440**, 89 (1985).
[6]H. A. Bethe, Phys. Rev. **53**, 675 (1938).
[7]R. Weiner and M. Weström, Nucl. Phys. **A286**, 282 (1977).
[8]G. D. Harp, J. M. Miller, and B. J. Berne, Phys. Rev. **165**, 1166 (1968).
[9]M. Blann, Phys. Rev. C **31**, 1245 (1985).
[10]B. G. Harvey, Nucl. Phys. **A444**, 498 (1985).
[11]J. Randrup and R. Vandenbosch, Nucl. Phys. **A474**, 219 (1987).
[12]L. G. Sobotka, Z. Majka, D. G. Sarantites, D. W. Stracener, V. Abenante, T. M. Semkow, D. C. Hensley, J. R. Beene, and M. L. Halbert, *Proceedings of the Symposium on Nuclear Dynamics and Nuclear Disassembly,* Dallas, Texas, 1989 (World Scientific, Singapore, 1989), p. 67.
[13]A. Chbihi, L. G. Sobotka, N. G. Nicolis, D. G. Sarantites, D. W. Stracener, Z. Majka, D. C. Hensley, J. R. Beene, and M. L. Halbert, Phys. Rev. C **43**, 666 (1991), the following paper.
[14]M. Jääskeläinin, D. G. Sarantites, R. Woodward, F. A. Dilmanian, J. T. Hood, R. Jääskeläinen, D. C. Hensley, M. L. Halbert, and J. H. Barker, Nucl. Instrum. Methods **204**, 385 (1983). The conversion from neutron fold to neutron multiplicity is done using a calibration deduced from an unpublished work by T. M. Semkow, D. G. Sarantites, and J. R. Beene. The conversion factor is approximately 1 due to an approximate cancellation of the effects of the intrinsic interaction probability and rescattering for evaporation neutrons.
[15]D. W. Stracener, D. G. Sarantites, L. G. Sobotka, J. Elson, J. T. Hood, Z. Majka, V. Abenante, A. Chbihi, and D. C. Hensley, Nucl. Instrum. Methods **A294**, 485 (1990).
[16]W. W. Wilcke, J. R. Birkelund, H. J. Wollersheim, A. D. Hoover, J. R. Huizenga, W. U. Schröder, and L. E. Tubbs, At. Data Nucl. Data Tables **25**, No. 5/6 (1980).
[17]See Ref. 12, p. 42.
[18]D. Hilscher, Nucl. Phys. **A471**, 77c (1987).
[19]M. B. Tsang, Y. D. Kim, N. Carlin, Z. Chen, R. Fox, C. K. Gelbke, W. G. Gong, W. G. Lynch, T. Murakami, T. K. Nayak, R. M. Ronningen, H. M. Xu, F. Zhu, L. Sobotka, D. Stracener, D. G. Sarantites, Z. Majka, V. Abenante, and H. Griffin, Phys. Lett. B **220**, 492 (1989).
[20]L. G. Sobotka, D. G. Sarantites, Ze Li, E. L. Dines, M. L. Halbert, D. C. Hensley, J. C. Lisle, R. P. Schmitt, Z. Majka, G. Nebbia, H. C. Griffin, and A. J. Sierk, Phys. Rev. C **36**, 2713 (1987).
[21]K. Möhring, T. Srokowski, D. H. E. Gross and H. Homeyer, Phys. Lett. B **203**, 210 (1988); K. Möhring (private communication).
[22]T. C. Awes, G. Poggi, C. K. Gelbke, B. B. Back, B. G. Glagola, H. Breuer, and V. E. Viola, Jr., Phys. Rev. C **24**, 89 (1981).
[23]R. Wada, D. Fabris, K. Hagel, G. Nebbia, Y. Lou, M. Gonin, J. B. Natowitz, R. BIllerey, B. Cheynis, A. Demeyer, D. Drain, D. Guinet, C. Pastor, L. Vagneron, K. Zaid, J. Alarja, A. Giorni, D. Heuer, C. Morand, B. Viano, C. Mazur, C. Ngô, S. Leray, R. Lucas, M. Ribrag, and E. Tomasi, Phys. Rev. C **39**, 497 (1989).